

# The Heavy Photon Search Test Detector

M. Battaglieri<sup>a</sup>, S. Boyarinov<sup>b</sup>, S. Bueltmann<sup>c</sup>, V. Burkert<sup>b</sup>, A. Celentano<sup>a</sup>, G. Charles<sup>f</sup>, W. Cooper<sup>d</sup>, C. Cuevas<sup>b</sup>, N. Dashyan<sup>e</sup>, R. DeVita<sup>a</sup>, C. Desnault<sup>f</sup>, A. Deur<sup>b</sup>, H. Egriyan<sup>b</sup>, L. Elouadrhiri<sup>b</sup>, R. Essig<sup>g</sup>, V. Fadeyev<sup>h</sup>, C. Field<sup>i</sup>, A. Freyberger<sup>b</sup>, Y. Gershtein<sup>j</sup>, N. Gevorgyan<sup>e</sup>, F.-X. Girod<sup>b</sup>, N. Graf<sup>i</sup>, M. Graham<sup>i</sup>, K. Griffioen<sup>k</sup>, A. Grillo<sup>h</sup>, M. Guidal<sup>f</sup>, G. Haller<sup>i</sup>, P. Hansson Adrian<sup>i,\*</sup>, R. Herbst<sup>i</sup>, M. Holtrop<sup>l</sup>, J. Jaros<sup>i</sup>, S. Kaneta<sup>b</sup>, M. Khandaker<sup>m</sup>, A. Kubarovsky<sup>n</sup>, V. Kubarovsky<sup>b</sup>, T. Maruyama<sup>i</sup>, J. McCormick<sup>i</sup>, K. Moffeit<sup>i</sup>, O. Moreno<sup>h</sup>, H. Neal<sup>i</sup>, T. Nelson<sup>i</sup>, S. Niccolai<sup>f</sup>, A. Odian<sup>i</sup>, M. Oriunno<sup>i</sup>, R. Paremuzyan<sup>e</sup>, R. Partridge<sup>i</sup>, S. K. Phillips<sup>l</sup>, E. Rauly<sup>f</sup>, B. Raydo<sup>b</sup>, J. Reichert<sup>j</sup>, E. Rindel<sup>f</sup>, P. Rosier<sup>f</sup>, C. Salgado<sup>m</sup>, P. Schuster<sup>o</sup>, Y. Sharabian<sup>b</sup>, D. Sokhan<sup>p</sup>, S. Stepanyan<sup>b</sup>, N. Toro<sup>o</sup>, S. Uemura<sup>i</sup>, M. Ungaro<sup>b</sup>, H. Voskanyan<sup>e</sup>, D. Walz<sup>i</sup>, L. B. Weinstein<sup>c</sup>, B. Wojtsekhowski<sup>b</sup>

<sup>a</sup>Istituto Nazionale di Fisica Nucleare, Sezione di Genova e Dipartimento di Fisica dell'Università, 16146 Genova, Italy

<sup>b</sup>Thomas Jefferson National Accelerator Facility, Newport News, Virginia 23606

<sup>c</sup>Old Dominion University, Norfolk, Virginia 23529

<sup>d</sup>Fermi National Accelerator Laboratory, Batavia, IL 60510-5011

<sup>e</sup>Yerevan Physics Institute, 375036 Yerevan, Armenia

<sup>f</sup>Institut de Physique Nucléaire, CNRS/IN2P3 and Université Paris Sud, Orsay, France

<sup>g</sup>Stony Brook University, Stony Brook, NY 11794-3800

<sup>h</sup>Santa Cruz Institute for Particle Physics, University of California, Santa Cruz, CA 95064

<sup>i</sup>SLAC National Accelerator Laboratory, Menlo Park, CA 94025

<sup>j</sup>Rutgers University, Department of Physics and Astronomy, Piscataway, NJ 08854

<sup>k</sup>The College of William and Mary, Department of Physics, Williamsburg, VA 23185

<sup>l</sup>University of New Hampshire, Department of Physics, Durham, NH 03824

<sup>m</sup>Norfolk State University, Norfolk, Virginia 23504

<sup>n</sup>Rensselaer Polytechnic Institute, Department of Physics, Troy, NY 12181

<sup>o</sup>Perimeter Institute, Ontario, Canada N2L 2Y5

<sup>p</sup>University of Glasgow, Glasgow, G12 8QQ, Scotland, UK

---

## Abstract

The Heavy Photon Search (HPS), an experiment to search for a hidden sector photon in fixed target electroproduction, is preparing for installation at the Thomas Jefferson National Accelerator Facility (JLab) in the Fall of 2014. As the first stage of this project, the HPS Test Run apparatus was constructed and operated in 2012 to demonstrate the experiment's technical feasibility and to confirm that the trigger rates and occupancies are as expected. This paper describes the HPS Test Run apparatus and readout electronics and its performance. In this setting, a heavy photon can be identified as a narrow peak in the  $e^+e^-$  invariant mass spectrum above the trident background or as a narrow invariant mass peak with a decay vertex displaced from the production target, so charged particle tracking and vertexing are needed for its detection. In the HPS Test Run, charged particles are measured with a compact forward silicon microstrip tracker inside a dipole magnet. Electromagnetic showers are detected in a PbWO<sub>4</sub> crystal calorimeter situated behind the magnet, and are used to trigger the experiment and identify electrons and positrons. Both detectors are placed close to the beam line and split top-bottom. This arrangement provides sensitivity to low-mass heavy photons, allow clear passage of the unscattered beam, and avoids the spray of degraded electrons coming from the target. The discrimination between prompt and displaced  $e^+e^-$  pairs requires the first layer of silicon sensors be placed only 10 cm downstream of the target. The expected signal is small, and the trident background huge, so the experiment requires very large statistics. Accordingly, the HPS Test Run utilizes high-rate readout and data acquisition electronics and a fast trigger to exploit the essentially 100% duty cycle of the CEBAF accelerator at JLab.

**Keywords:** silicon, microstrip, tracking, vertexing, heavy photon, dark photon, electromagnetic calorimeter

---

1    **1. Introduction**

2    The heavy photon ( $A'$ ), aka a “hidden sector” or  
3    “dark” photon, is a massive gauge boson which couples  
4    weakly to electric charge by mixing with the Standard  
5    Model photon [1, 2]. Consequently, it can be radiated  
6    by electrons and subsequently decay into  $e^+e^-$  pairs, al-  
7   beit at rates far below those of QED trident processes.  
8    Heavy photons have been suggested by numerous be-  
9   yond Standard Model theories [3] to explain the discrep-  
10   ancy between theory and experiment of the muon’s  $g-2$   
11   [4], and as a possible explanation of recent astrophysical  
12   anomalies, e.g. [5, 6, 7]. Heavy photons couple directly  
13   to hidden sector particles with “dark” or “hidden sec-  
14   tor” charge; these particles could constitute all or some  
15   of the dark matter, e.g. [8, 9]. Current phenomenology  
16   highlights the  $20 - 1000 \text{ MeV}/c^2$  mass range, and sug-  
17   gests that the coupling to electric charge,  $\epsilon e$ , has  $\epsilon$  in the  
18   range of  $10^{-3} - 10^{-5}$ . This range of parameters makes  
19    $A'$  searches viable in medium energy fixed target elec-  
20   troproduction [10], but requires large data sets and good  
21   mass resolution to identify a small mass peak above the  
22   copious QED background. At small couplings, the  $A'$   
23   becomes long-lived, so detection of a displaced decay  
24   vertex can reject the prompt QED background and boost  
25   experimental sensitivity.

26    The HPS experiment [11] is preparing for installation  
27   in Hall-B at JLab in the Fall of 2014 to search for heavy  
28   photons by directing the 2.2-6.6 GeV CEBAF12 elec-  
29   tron beam onto a thin ( $0.25\% X_0$ ) Tungsten target foil.  
30    The HPS experiment uses both invariant mass and sec-  
31   ondary vertex signatures to search for  $A'$  decays into  
32    $e^+e^-$  pairs. At CEBAF energies, the  $A'$  decay products  
33   are boosted along the beam axis with small opening an-  
34   gles. For couplings  $\epsilon \ll 10^{-3}$ ,  $A'$  decay lengths range  
35   from millimeters to tens of centimeters and beyond. Ac-  
36   cordingly the tracking detectors cover opening angles  
37   down to 15 mrad and are placed just 10 cm downstream  
38   of the target.

39    HPS employs a 90 cm long silicon tracking and  
40   vertexing detector located inside a dipole magnet to  
41   measure momenta and decay vertex positions. A fast  
42   PbWO<sub>4</sub> electromagnetic calorimeter downstream of the  
43   magnet provides the trigger and electron identification.  
44    Both the silicon tracker and the ECal have  $\sim$ ns tim-  
45   ing resolution, which eliminates much of the out-of-  
46   time background from multiple scattered beam elec-  
47   trons. Fast front end electronics and high trigger and

48    data rate capability and the effectively 100% duty cycle  
49   of the CEBAF accelerator allows HPS to accumulate the  
50   very large statistics needed to be sensitive to the highly  
51   suppressed production of heavy photons.

52    The HPS Test Run, using a simplified version of the  
53   HPS apparatus, was proposed and approved at JLab as  
54   the first stage of HPS. Its purposes included demonstra-  
55   ting that the apparatus and data acquisition systems are  
56   technically feasible and the trigger rates and occupan-  
57   cies to be encountered in electron-beam running are as  
58   simulated. Given dedicated running time with electron  
59   beams, the HPS Test Run apparatus is capable of search-  
60   ing for heavy photons in unexplored regions of param-  
61   eter space. Therefore, key design criteria and require-  
62   ments for HPS and the HPS Test Run apparatus are the  
63   same:

- 64   • uniform acceptance between 15 and approximately  
65   70 mrad in the forward region to catch boosted de-  
66   cay products close to the beam,
- 67   • beam passage through the apparatus in vacuum, to  
68   eliminate direct interactions with the detector and  
69   minimize beam gas interactions,
- 70   • detector components that can survive and effi-  
71   ciently operate in a high radiation environment  
72   with some localized doses at the 100 Mrad level,
- 73   • high-rate electronics, handling trigger rates up to  
74   50 kHz and data rates of 100 MB/s to permanent  
75   storage,
- 76   • a flexible, redundant and efficient trigger for select-  
77   ing electron and positron pairs, capable of handling  
78   rates up to 50 kHz,
- 79   • hit reconstruction efficiency higher than 99% and  
80   average track reconstruction efficiency higher than  
81   98% for electrons and positrons,
- 82   • 2 ns hit time resolution in the silicon vertex tracker,
- 83   •  $A'$  mass resolution of 2.5% or better, which trans-  
84   lates to momentum resolution of 4.5% and angular  
85   resolution 2 mrad/ $p(\text{GeV}/c)$  for  $B=0.5 \text{ T}$ ,
- 86   • resolution of distance of closest approach to the  
87   beam axis less than 250 (100)  $\mu\text{m}$  for tracks with  
88   0.5 (1.7)  $\text{GeV}/c$ . This gives a decay length resolu-  
89   tion of about 1 mm for a 100  $\text{MeV}/c^2 A'$ .
- 90   • PbWO<sub>4</sub> electromagnetic calorimeter energy reso-  
91   lution  $\Delta E/E \leq 5\%/\sqrt{E}$  and transverse segmentation  
92    $\sim 1.5 \text{ cm}$  (< Moliere radius in PbWO<sub>4</sub>). The en-  
93   ergy resolution requirement for triggering is less

---

\*Corresponding author.

Email address: phansson@slac.stanford.edu (P. Hansson Adrian)

94 stringent because the electrons and positrons have  
95  $E > 0.5$  GeV. The segmentation provides good  
96 spatial resolution and guarantees minimal shower  
97 overlap with background hits.

98 The HPS Test Run apparatus was installed on April  
99 19, 2012, and ran parasitically in the photon beam of  
100 the HDice experiment [12] until May 18. The JLab run  
101 schedule precluded any dedicated electron beam run-  
102 ning, but the HPS Test Run was allowed an eight hour  
103 dedicated photon beam run at the end of scheduled CE-  
104 BAF running. During this dedicated period,  $e^+e^-$  pairs,  
105 produced in a gold foil upstream of the experiment,  
106 were studied. With no dedicated electron beam run-  
107 ning, it was not possible to search for an  $A'$ . However,  
108 the final running provided enough data to demonstrate  
109 the functionality of the apparatus, document its perfor-  
110 mance, and explore trigger rates, as shown below.

111 This paper reviews the HPS Test Run apparatus, doc-  
112 umenting the performance of the trigger, data acquisi-  
113 tion, silicon tracking and vertex detector, and the elec-  
114 tromagnetic calorimeter at, or close to, the level re-  
115 quired for the HPS experiment.

## 116 2. Detector Overview

117 The HPS Test Run apparatus was designed to run  
118 in Hall B at JLab using the CEBAF 499MHz electron  
119 beam at energies between 2.2 and 6.6 GeV and cur-  
120 rents between 200 and 600 nA. The overall design of  
121 the experiment follows from the kinematics of  $A'$  pro-  
122 duction which typically results in a final state particle  
123 within a few degrees of the incoming beam, especially  
124 at low  $m_{A'}$ . Detectors must therefore be placed close  
125 to the beam. The intense electron beam enlarges down-  
126 stream after multiple scattering in the target and elec-  
127 trons which have radiated in the target disperse horizon-  
128 tally in the field of the analyzing magnet. Together they  
129 constitute a “wall of flame” which must be completely  
130 avoided. Accordingly, the apparatus is split vertically  
131 to avoid a “dead zone”, the region within  $\pm 15$  mrad of  
132 the beam plane. In addition, the beam is transported in  
133 vacuum through the tracker to minimize beam-gas inter-  
134 action backgrounds. Even with these precautions, the  
135 occupancies of sensors near the beam plane are high,  
136 dominated by the multiple Coulomb scattering of the  
137 primary beam, so high-rate detectors, a fast trigger, and  
138 excellent time tagging are required to minimize their  
139 impact. The trigger comes from a highly-segmented  
140 lead-tungstate ( $PbWO_4$ ) crystal calorimeter located just  
141 downstream of the dipole magnet.

143 A rendering of the apparatus installed on the beam line  
144 is shown in Figure 1 and an overview of the coverage,  
145 segmentation and performance is given in Table 1.

146 The silicon tracking and vertexing detector for the  
147 HPS Test Run, or SVT, resides in a vacuum cham-  
148 ber inside the Pair Spectrometer (PS) dipole magnet in  
149 Hall B at JLab. The magnetic field strength was 0.5 T  
150 oriented vertically throughout the run. The SVT has  
151 five measurement stations, or “layers,” beginning 10 cm  
152 downstream of the target. Each layer comprises a pair  
153 of closely-spaced silicon microstrip sensors responsi-  
154 ble for measuring a single coordinate, or “view”. In-  
155 troduction of a small (50 or 100 mrad) stereo angle  
156 between the two sensors of each layer provides three-  
157 dimensional tracking and vertexing throughout the ac-  
158 ceptance of the detector. In order to accommodate the  
159 dead zone, the SVT is built in two halves that are ap-  
160 proximately mirror reflections of one another about the  
161 plane of the nominal electron beam. Each layer in one  
162 half is supported on a common support plate with inde-  
163 pendent cooling and readout.

164 The electromagnetic calorimeter (ECal) is also split  
165 into two halves. Each half of the ECal consists of  
166 221  $PbWO_4$  crystals arranged in rectangular formation.  
167 There are five rows with 46 crystals in each row except  
168 the row closest to the beam plane which has 37. The  
169 light from each crystal is read out by an Avalanche Photo-  
170 diode (APD) glued on the back surface of the crys-  
171 tal. Signals from the APDs are amplified using custom-  
172 made amplifier boards before being sent to the data ac-  
173 quisition electronics.

174 The Data Acquisition system combines two architec-  
175 tures, the Advanced Telecom Communications Archi-  
176 tecture (ATCA) based SVT readout system and VME-  
177 bus Switched Serial (VXS) based digitization and trig-  
178 gering system for the ECal.

## 179 3. The HPS Test Run Beamline

180 Since an electron beam was unavailable, the HPS Test  
181 Run detected the electrons and positrons produced by  
182 interactions of the secondary photon beam with a thin  
183 foil just upstream of the detectors. The HPS Test Run  
184 studied the performance of the detectors and the mul-  
185 tiple coulomb scattering of the electrons and positrons.  
186 Figure 2 shows the layout of the setup on the beam line.  
187 The SVT was installed inside the Hall B pair spectrom-  
188 eter magnet vacuum chamber with the ECal mounted  
189 downstream of it. Both the SVT and the ECal were re-  
190 tracted off the beam plane compared to nominal electron  
191 beam running to allow clean passage of the photon beam  
192 through the system.

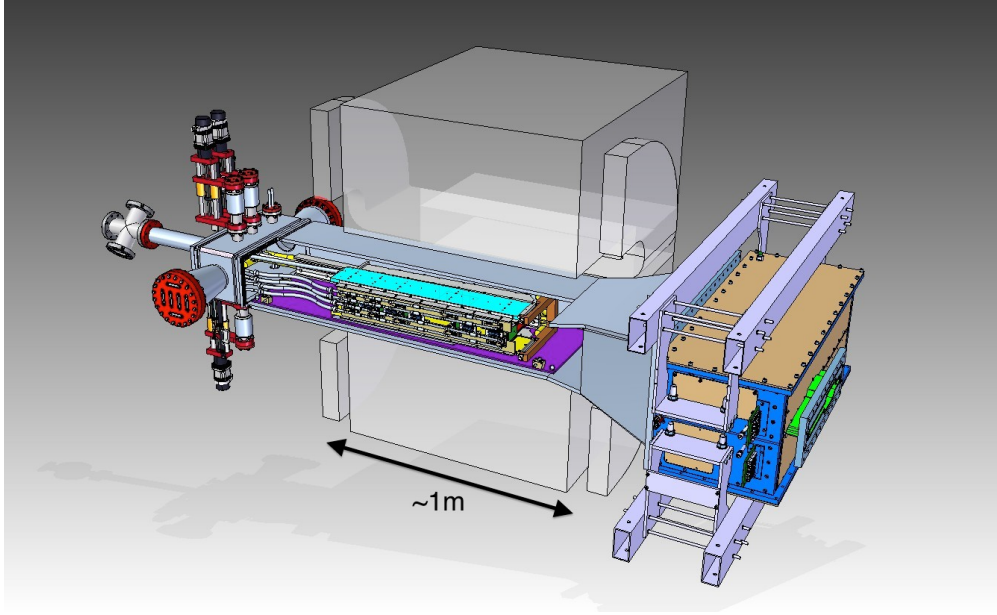


Figure 1: Rendering of the HPS Test Run apparatus installed on the beam line.

Table 1: Overview of the coverage, segmentation and performance of the HPS Test Run detector. The  $\sigma_{d_0}$  is the track impact parameter resolution of the SVT at the nominal electron target position.  $\sigma_{pos}$  is the estimated position resolution perpendicular to the strip direction on the silicon sensors of the SVT.

| System | Coverage (mrad)                  | # channels | ADC (bit) | # layers             | Segmentation   | Time resolution (ns) | Performance  |
|--------|----------------------------------|------------|-----------|----------------------|--|----------------------|--|
| SVT    | $15 < \theta_y < 70$<br>(5 hits) | 12780      | 14        | 5<br>(stereo layers) | $30 \mu\text{m}$ (sense)<br>$60 \mu\text{m}$ (readout)<br>( $\sigma_{pos} \approx 6 \mu\text{m}$ ) | 2.5                  | $\sigma_{d0,y} \approx 100 \mu\text{m}$<br>$\sigma_{d0,x} \approx 300 \mu\text{m}$<br>$\sigma_{d0,z} \approx 1 \text{ mm}$ |
| ECal   | $15 < \theta_y < 60$             | 442        | 12        | 1                    | $1.33 \times 1.33 \text{ cm}^2$<br>$1.6 \times 1.6 \text{ cm}^2$                                   | 4<br>(trigger)       | $\sigma(E)/E \approx 4.5\%/\sqrt{E}$<br>Ref. [13, 14, 15]  |

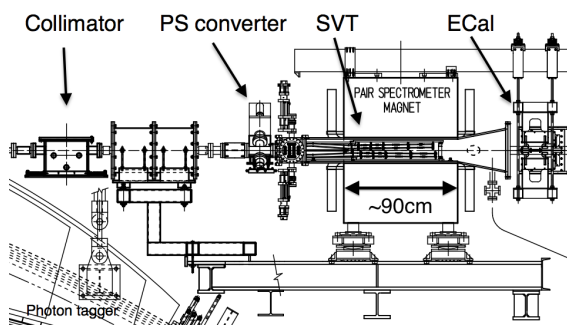


Figure 2: Layout of the HPS parasitic run.

The photon beam was generated in the interaction of 5.5 GeV electrons with a  $10^{-4} X_0$  gold radiator located  $\approx 9$  m upstream of the PS. The primary beam and scattered electrons are deflected away from detectors by the dipole magnet of the photon tagging system. During the dedicated HPS Test Run period, the collimated (6.4 mm diameter) photon beam passes through the PS pair converter gold foil and later the HPS system. The PS pair converter was located  $\approx 77$  cm upstream of the first layer of the SVT.

Data was taken on three different converter thicknesses with photon fluxes between 0.4 and  $1.3 \times 10^8/\text{s}$  at photon energies between 0.55 and 5.5 GeV produced by a 30 to 90 nA electron beam. Data was measured for both polarities of the PS dipole magnet. The photon beam line during the HPS Test Run produced a relatively large number of  $e^+e^-$  pairs originating upstream

| Converter thickn.<br>(% $X_0$ ) | Duration<br>(s) | $e^-$ on radiator<br>( $\mu$ C) |
|---------------------------------|-----------------|---------------------------------|
| 0                               | 1279            | 88.1                            |
| 0.18                            | 2640            | 193.5                           |
| 0.45                            | 2149            | 140.7                           |
| 1.6                             | 911             | 24.4                            |

Table 2: Measured integrated currents for the dedicated photon runs.

of the converter position. This contribution was measured during data taking with “empty” converter runs, i.e. removing the converter but with all other conditions the same. The runs taken during the time dedicated to HPS Test Run are summarized in Table 2.

#### 4. Silicon Vertex Tracker

The Silicon Vertex Tracker (SVT) enables efficient reconstruction of charged particles and precise determination of their trajectories. This allows  $A'$  decays to be distinguished from background via simultaneous measurements of the invariant mass of  $e^+e^-$  decay products and the position of decay vertices downstream of the target.

The design of the SVT is primarily driven by physics requirements and constraints from the environment at the interaction region. The  $A'$  decay products have momenta in the range of 0.4-2.0 GeV/c (from a 2.2 GeV beam), so multiple scattering dominates mass and vertexing uncertainties for any possible material budget. The SVT must therefore minimize the amount of material in the tracking volume. The signal yield for long-lived  $A'$  is very small, so the rejection of prompt vertices must be exceedingly pure, on the order of  $10^{-7}$ , in order to eliminate all prompt backgrounds. To achieve the required vertexing performance the first layer of the SVT must be placed no more than about 10 cm downstream of the target. At that distance, it is found that the active region of a sensor can be placed as close as 1.5 mm from the center of the beam, defining the 15 mrad “dead zone” mentioned previously, to maximize low-mass  $A'$  acceptance with decay products nearly collinear with the beam axis. At the edge of this “dead zone”, the radiation dose approaches  $10^{15}$  electrons/cm<sup>2</sup>/month, or roughly  $3 \times 10^{14}$  1 MeV neutron equivalent/cm<sup>2</sup>/month [16], requiring the sensors to be actively cooled. Meanwhile, very low-energy delta rays from beam-gas interactions would multiply the density of background hits, so the SVT must operate inside the beam vacuum. Finally, in order to protect the sensors, the detector must be movable

so that it can be retracted during periods of uncertain beam conditions or beam tuning.

A mass resolution of 2.5% is adequate to extend a bump-hunt search for an  $A'$  into virgin territory. For running at 2.2 GeV, this translates into a requirement for track momentum ( $p$ ) resolution of 4-5% and angular resolution of 2 mrad/ $p$ (GeV/c) [11]. Multiple coulomb scattering dominates both the mass and vertexing uncertainties, relaxing the spatial hit resolution requirement to  $< 100 \mu\text{m}$  ( $50 \mu\text{m}$ ) in the bend (non-bend) plane.

High background occupancies, up to 4 MHz/mm<sup>2</sup> locally, in the region closest to the beam result from beam electrons undergoing multiple scattering in the target. These background hits are rejected by requiring the time reconstruction of each hit to be better than 2 ns.

##### 4.1. Layout

The layout of the SVT is summarized in Table 3 and rendered in Figure 3. Each of the layers is comprised of a pair of closely-spaced silicon microstrip sensors mounted back-to-back to form a module. A 100 mrad stereo angle is used in the first three layers to provide higher-resolution 3D space points for vertexing. Using 50 mrad in the last two layers breaks the tracking degeneracy of having five identical layers and minimizes fakes from ghost hits to improve pattern recognition. Altogether, the SVT has 20 sensors for a total of 12780 readout channels.

| Layer                           | 1            | 2            | 3            | 4             | 5             |
|---------------------------------|--------------|--------------|--------------|---------------|---------------|
| $z$ from target (cm)            | 10           | 20           | 30           | 50            | 70            |
| Stereo angle (mrad)             | 100          | 100          | 100          | 50            | 50            |
| Bend res. ( $\mu\text{m}$ )     | $\approx 60$ | $\approx 60$ | $\approx 60$ | $\approx 120$ | $\approx 120$ |
| Non-bend res. ( $\mu\text{m}$ ) | $\approx 6$  | $\approx 6$  | $\approx 6$  | $\approx 6$   | $\approx 6$   |
| # of sensors                    | 4            | 4            | 4            | 4             | 4             |
| Dead zone (mm)                  | $\pm 1.5$    | $\pm 3.0$    | $\pm 4.5$    | $\pm 7.5$     | $\pm 10.5$    |
| Power cons. (W)                 | 6.9          | 6.9          | 6.9          | 6.9           | 6.9           |

Table 3: Layout of the SVT.

The SVT is built in two separate halves that are mirror reflections of one another about the plane of the nominal electron beam. Each half consists of five modules mounted on a support plate that provides services to the modules and allows them to be moved as a group relative to the dead zone. The two halves of the tracker are connected to hinges mounted on a C-shaped support just beyond the last layer that defines the nominal spacing between the upper and lower halves of the tracker.

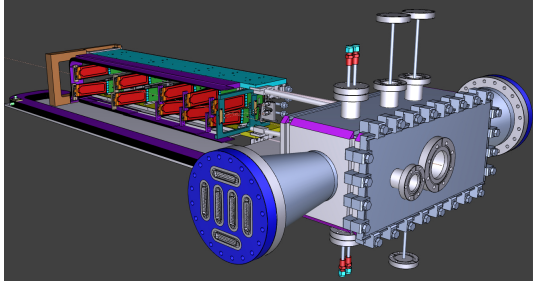


Figure 3: A rendering of the SVT showing the modules on their support plates held by the hinged C-support on the left and the motion levers on the right. The sensors are shown in red and the hybrid readout boards in green. The beam enters from the right through a vacuum box with flanges for services.

A shaft attached to each support plate in front of layer one extends upstream and connects to a linear shift that transfers motion into the vacuum box through bellows to open and close the two halves around the dead zone. The C-support is mounted to an aluminum baseplate that defines the position of the SVT with respect to the vacuum chamber. Figure 4 shows a photograph of both completed detector halves prior to final assembly.



Figure 4: Both halves of the HPS Test Run SVT after final assembly at SLAC. The cooling manifolds and integrated cable runs are clearly seen.

295

#### 296 4.2. Components

The sensors for the SVT are  $p+$ -on- $n$ , single-sided, AC-coupled, polysilicon-biased microstrip sensors fabricated on  $<100>$  silicon and have 30 (60)  $\mu\text{m}$  sense (readout) pitch over their  $4 \times 10 \text{ cm}^2$  surface. This sensor technology was selected to match the requirement of  $< 1\% X_0$  per layer, single-hit resolution better than 50  $\mu\text{m}$  and tolerance of a radiation dose of approximately  $1.5 \times 10^{14} 1 \text{ MeV neutron equivalent}/\text{cm}^2$

305 for a six month run. The sensors, produced by Hamamatsu Photonics Corporation, were originally meant  
306 for the cancelled Run 2b upgrade of the DØ experiment [17] which satisfied the requirement that the  
307 technology must be mature and available within the time and  
308 budget constraints.  
309

310 Despite having only small spots with very high occupancy (up to 4 MHz/mm<sup>2</sup>) closest to the primary beam,  
311 the rates are still high and lowering the peak occupancy  
312 to approximately 1% for tracking requires a trigger window  
313 and hit time tagging of roughly 8 ns. The ECal  
314 readout and trigger described in Sec. 5.3 can achieve  
315 such resolution. To reach this performance the sen-  
316 sors for the SVT are readout by the APV25 ASIC de-  
317 veloped for the CMS experiment at CERN [18]. The  
318 APV25 can capture successive samples of the shaper  
319 output in groups of three at a sampling rate of approx-  
320 imately 40 MHz. By fitting the known CR-RC shaping  
321 curve to these samples, the initial time of the hit can  
322 be determined to a precision of 2 ns for S/N≈25 [19].  
323 For electron beam running, six-sample readout and the  
324 shortest possible shaping time (35 ns) is used to best  
325 distinguish hits that overlap in time. The APV25 ASICS  
326 are hosted on simple FR4 hybrid readout boards, out-  
327 side the tracking volume, with a short twisted-pair pig-  
328 tail cable to provide power and configuration and signal  
329 readout. Along with a single sensor, these are glued  
330 to a polyimide-laminated carbon fiber composite back-  
331 ing making up a half-module. A window is machined  
332 in the carbon fiber leaving only a frame around the pe-  
333 riphery of the silicon to minimize material. A 50  $\mu\text{m}$   
334 sheet of polyamide is laminated to the surface of the  
335 carbon fiber with 1 mm overhang at all openings to en-  
336 sure good isolation between the back side of the sensor,  
337 carrying high-voltage bias, and the carbon fiber which  
338 is held near ground.  
339

340 The sensor modules for the SVT consist of a pair  
341 of identical half-modules, sandwiched back-to-back  
342 around an aluminum cooling block at one end and a sim-  
343 ilar PEEK spacer block at the other. Figure 5 shows a  
344 single module after assembly. The cooling block pro-  
345 vides the primary mechanical support for the module as  
346 well as cooling via copper tubes pressed into grooves  
347 in the plates. The spacer block defines the spacing be-  
348 tween the sensors at the far end of the module, stiffens  
349 the module structure, and improves the stability of the  
350 sensor alignment. The average support material in the  
351 tracking volume is approximately 0.06%  $X_0$  per double-  
352 sided module for a total material budget of 0.7% per  
353 layer.  
354

The total SVT power consumption budget of about 50 W is removed by a water/glycol mixture circulated

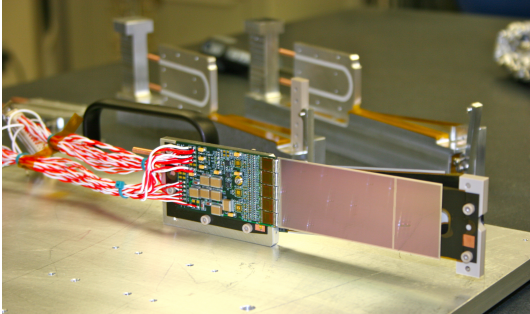


Figure 5: A prototype module assembly (foreground) with the 50 mrad (left) and 100 mrad (right) module assembly fixtures in the background. A pair of cooling blocks and a spacer block can be seen on the fixtures.

through a flexible manifold attached to the copper tubes in the cooling blocks. During the HPS Test Run the sensors were operated at around 23° C. The power consumption is dominated by five APV25 ASICs on each hybrid board consuming approximately 2 W, the radiant heat load is less than 0.5 W per sensor and leakage current is only significant in a small spot after irradiation.

#### 4.3. Production, Assembly and Shipping

Hybrids with APV25 ASICs underwent quick qualification testing and each half-module was run at low temperature ( $\approx 5^\circ \text{C}$ ) and fully characterized for pedestals, gains, noise and time response after assembly. Of 29 half-modules built, 28 passed qualification testing, leaving eight spare modules after completion of the SVT. Only sensors capable of 1000 V bias voltage without breakdown were used. Full-module assembly and mechanical surveys were performed at SLAC before final assembly, testing and shipping of the SVT to JLab. A custom shipping container with nested crates and redundant isolation for shock and vibration was built in order to safely send the partly assembled SVT to JLab. At JLab, the entire SVT was integrated with the full DAQ and the power supplies before moving the module-loaded support plates to Hall B for final mechanical assembly and installation inside of the vacuum chamber.

#### 4.4. Alignment

The SVT was aligned using a combination of optical, laser and touch probe surveys at SLAC and JLab. The optical survey of individual modules with a precision of a few  $\mu\text{m}$  was combined with a touch-probe survey of the overall SVT support structure, with 25-100  $\mu\text{m}$  precision, to locate the silicon sensor layers with respect

to the support plates and the mechanical survey balls on the base plate. After full assembly and installation of the SVT at JLab, a mechanical survey of the SVT base plate position inside the pair spectrometer vacuum chamber is used to determine the global position of the SVT with respect to the CEBAF beam line. The resulting survey-based alignment has the position of the silicon sensors correct to within a few hundred microns measured from tracks in the HPS Test Run data. A more sophisticated global track-based alignment technique to reach final alignment precision well below 50  $\mu\text{m}$  is being developed.

## 5. Electromagnetic Calorimeter

The electromagnetic calorimeter (ECal), installed downstream of the PS dipole magnet, performs two essential functions for the experiment: it provides a trigger signal to select what events to read out from the detector sub-systems and is used to identify electrons and positrons. The technology and design choices are largely driven by the need for a compact forward design covering the SVT A' acceptance and able to measure the energy and positions of electrons and positrons with energy between 0.5-6.5 GeV. It needs granularity and signal readout speed to handle 1 MHz/cm<sup>2</sup> of electromagnetic background and radiation hardness. Even modest energy resolution is adequate for triggering. HPS requires better energy resolution,  $\sigma(E)/E < 5\%/\sqrt{E}$ , so that the ECal energy measurement can be used in combination with that from the SVT to improve the overall momentum resolution.

The PbWO<sub>4</sub> crystal inner calorimeter of the CLAS detector [13, 14, 15], in operation since 2005 in Hall B, meets all the requirements set by HPS. The modules from this calorimeter have been subsequently repurposed for HPS.

### 5.1. Components

The ECal module shown in Figure 6 is based on a tapered 160 mm long PbWO<sub>4</sub> crystal with a 13.3 × 13.3 mm<sup>2</sup> (16 × 16 mm<sup>2</sup>) front (rear) face wrapped in VM2000 multilayer polymer mirror film. The scintillation light yield, approximately 120 photons/MeV, is read out by a 5×5 mm<sup>2</sup> Hamamatsu S8664-55 Avalanche Photodiode (APD) with 75% quantum efficiency glued to the rear face surface using MeltMount 1.7 thermal plastic adhesive. This results in about eight photoelectrons/MeV which needs to be amplified before being fed into the FADC for digitization and processing. The maximum energy deposited in a crystal is expected to be 4.2 GeV which needs to match the input

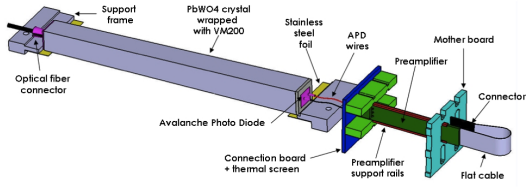


Figure 6: A schematic view of an ECal module.

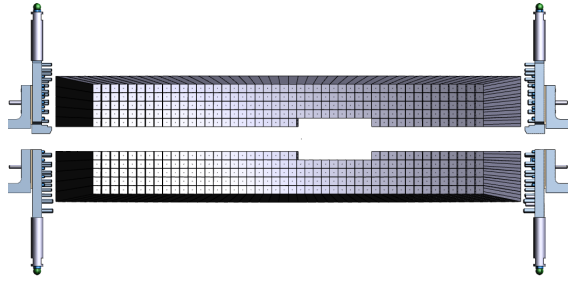


Figure 7: Rendered layout view of the ECal looking downstream.

range of the FADC. The relatively low gain of the APD (~200) was compensated with custom-made preamplifier boards, that provide further amplification to match the 2 V dynamic range of the FADC. The ADC has 12-bit resolution. Gains are adjusted to give about 1 ADC count/MeV. This dynamic range is adequate to measure the 10 MeV noise level as well as the the maximum energy expected in a single crystal, about 4 GeV.

### 5.2. Layout

Similar to the SVT, the ECal is built in two separate halves that are mirror reflections of one another about the plane of the nominal electron beam to avoid interfering with the 15 mrad “dead zone”. As shown in Figure 7, the 221 modules in each half, supported by aluminum support frames, are arranged in rectangular formation with five layers and 46 crystals/layer except for the layer closest to the beam where nine modules were removed to allow a larger opening for the outgoing electron and photon beams. Each half was enclosed in a temperature controlled box ( $< 1^\circ \text{F}$  stability and  $< 4^\circ \text{F}$  uniformity) to stabilize the crystal light yield and the operation of the APDs and its preamplifiers. Four printed circuit boards mounted on the backplane penetrated the enclosure and were used to supply the  $\pm 5$  V operating voltage for the preamplifiers, 400 V bias voltage to the APDs, and to read out signals from the APDs. Each half of the ECal was divided into 12 bias voltage groups with a gain uniformity of about 20%.

During the HPS Test Run, both halves were held in place by four vertical bars attached to a rail above, placing the front face of the crystals 147 cm from the upstream edge of the magnet, with a 8.7 cm gap between the innermost edge of the crystals in the two halves.

### 5.3. Signal readout

After a 2:1 signal splitter, 1/3 of an amplified APD signal was fed to a single channel of a JLab flash ADC (FADC) board [20]. 2/3 of the signal was sent to a discriminator module and then to a TDC for a timing measurement. The FADC boards are high speed VXS

modules digitizing up to 16 APD signals at 250 MHz and storing samples in  $8 \mu\text{s}$  deep pipelines with 12-bit resolution. When a trigger is received, the part of the pipeline from five samples before and 30 after the signal which crossed a programmable threshold (for the HPS Test Run this was set to  $\approx 70$  MeV) are summed and stored in a 17-bit register for readout. In addition a 4 ns resolution timestamp of the threshold crossing is reported in the readout for each pulse. This scheme significantly compresses the data output of the FADC. During offline data analysis, a calibrated pedestal value is subtracted to obtain the actual summed energy. Two 20-slot VXS crates with 14 (13) FADC boards were employed in the HPS Test Run to read out the top (bottom) half of the ECal.

## 6. Trigger and Data Acquisition

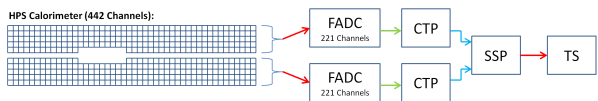
The DAQ system handles acquisition of data from the ECal and SVT sub-detectors with two DAQ architectures. The SVT DAQ is based on Advanced Telecom Communications Architecture (ATCA) hardware while the ECal uses VMEbus Switched Serial (VXS) based hardware. Data from the sub-detectors are only read out when a trigger signal from the trigger system is received.

### 6.1. Trigger system

The trigger system is designed to select time coincidences of electromagnetic clusters in the top and bottom halves of the ECal which satisfy kinematic conditions satisfied by  $A'$  decays and minimize backgrounds. The trigger system needs to be essentially dead-time free, handle rates up to 50 kHz, and supply a trigger signal which jitters  $< 8$  ns from the actual event time in order to minimize backgrounds from out-of-time hits in the SVT. Figure 8 shows a schematic overview of each

511 stage of the system. Each channel on the FADC board  
 512 has an independent data path to send 5-bit pulse energy  
 513 and 3-bit pulse arrival time information every 32 ns to  
 514 a trigger processing board (CTP), which is in the same  
 515 crate. The 3-bit pulse arrival time allows the trigger to  
 516 know the pulse timing at 4 ns resolution. Contrary to  
 517 the readout path described in Sec. 5.3, this energy is a  
 518 pedestal-subtracted time-over-threshold sum with pro-  
 519 grammable offsets and minimum threshold discrimina-  
 520 tor for each channel. With input from all FADC chan-  
 521 nels, i.e. one half of the ECal, the CTP performs cluster  
 522 finding and calculates cluster energy and timing infor-  
 523 mation. The 3x3 fixed-window, highly parallel, FPGA-  
 524 based cluster algorithm simultaneously searches for up  
 525 to 125 clusters with energy sum larger than the pro-  
 526 grammable energy threshold set to about 270 MeV. This  
 527 high threshold didn't hurt the trigger rate rate studies  
 528 for the HPS Test run since only clusters with high ener-  
 529 gies were studied but for HPS this threshold will need to  
 530 be lower. Crystals in the fixed-window are included in  
 531 the sum if the leading edge of the pulse occurred within  
 532 a 32 ns time window to take into account clock skew  
 533 and jitter throughout the system. The CTP only accepts  
 534 clusters with the locally highest energy 3x3 window to  
 535 deal with overlapping and very large clusters. The sub-  
 536 system board (SSP) receives the clusters from the top  
 537 and bottom half CTP at a maximum of 250MHz and  
 538 searches for pairs of clusters in an 8 ns wide coinci-  
 539 dence window. The SSP sends triggers to the trigger su-  
 540 pervisor (TS), which generates all the necessary signals  
 541 and controls the entire DAQ system readout through the  
 542 trigger interface units installed in every crate that par-  
 543 ticipate in the readout process.

544 The trigger system is free-running and driven by the  
 545 250 MHz global clock and has essentially zero dead  
 546 time at the occupancies expected for HPS. The trigger  
 547 supervisor can apply dead time if necessary, for example  
 548 on a ‘busy’ or ‘full’ condition from the front-end elec-



549 Figure 8: Block diagram of the ECAL trigger system consisting  
 550 of the FADC that samples and digitizes signals for each detec-  
 551 tor channel and sends them for cluster finding in the CTP.  
 552 The CTP clusters are sent to the SSP where the final trigger de-  
 553 cision is taken based on pairs of clusters in both halves of the  
 554 ECal. The decision is sent to the Trigger Supervisor (TS) that  
 555 generates the necessary signals to read out the sub-detectors.



556 Figure 9: The SVT DAQ COB board with four data processing  
 557 daughter cards (DPMs) visible on the left side.

558 tronics. The system is designed to handle trigger rates  
 559 above 50 kHz and has a latency set to  $\approx 3 \mu\text{s}$  to match  
 560 that required by the SVT APV25 ASIC.

561 During the HPS Test Run, for the most part the trigger  
 562 system required only a single cluster in either the top or  
 563 bottom ECal halves but was tested to trigger rates above  
 564 100 kHz by lowering thresholds.

## 6.2. SVT Data Acquisition

565 The purpose of the SVT DAQ is to support the con-  
 566 tinuous 40 MHz readout and processing of signals from  
 567 each of the 20 silicon strip sensors of the SVT. The data  
 568 for each strip channel, six samples of the signal, needs  
 569 to be transferred to the JLab DAQ for those events se-  
 570 lected by the trigger at rates up to 50 kHz and with data  
 571 transfer rates up to 100 MB/s.

572 The SVT DAQ is based on the Reconfigurable Clus-  
 573 ter Element (RCE) and cluster interconnect concept de-  
 574 veloped at SLAC as generic building blocks for DAQ  
 575 systems. The RCE is a generic computational build-  
 576 ing block, housed on a separate daughter card called  
 577 Data Processing Module (DPM), that is realized on an  
 578 ATCA front board called the Cluster On Board (COB),  
 579 see Figure 9. The first generation RCE used in the HPS  
 580 Test Run consisted of a Virtex 5 FPGA with 1 GB of  
 581 DDR3 RAM. A schematic overview of the system is  
 582 shown in Figure 10. The analog outputs of up to 12  
 583 SVT half-modules (60 APV25 ASICs) are digitized on  
 584 the Rear-Transition-Module (RTM), a custom board on  
 585 the back side of the ATCA crate, interfacing the HPS-  
 586 specific readout to the generic DAQ components on the  
 587 COB. A pre-amplifier converts the APV25 differential  
 588 current output to a different voltage output scaled to the  
 589 sensitive range of a 14-bit ADC operating at the system  
 590 clock of 41.667 MHz. The RTM is organized into four  
 591 sections with each section supporting three SVT half-  
 592 module hybrids (15 APV25 ASICs). The RTM also in-  
 593 cludes a 4-channel fiber-optic module and supporting

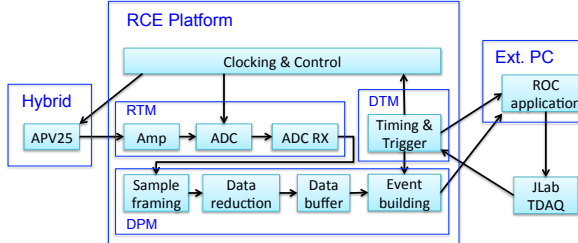


Figure 10: Block diagram overview of the SVT DAQ.

logic which is used to interface to the JLab trigger system supervisor. Each section of the RTM is input to a DPM which apply thresholds for data reduction and organizes the sample data into UDP datagrams. The DPM also hosts an I<sup>2</sup>C controller used to configure and monitor the APV25 ASICs. A single ATCA crate with two COB cards was used, one supporting four DPMs and one supporting three DPMs and one DPM that is configured as the trigger and data transmission module. The two COB cards and their DPMs are interconnected with a 10 Gb/s switch card [21] which also hosts two 1Gb/s Ethernet interfaces to the external SVT DAQ PC.

The external PC supports three network interfaces: two standard 1 Gb/s Ethernet and one custom low-latency data reception card. The first is used for slow control and monitoring of the 8 DPM modules and the second serves as the interface to the JLAB data acquisition system. The third custom low-latency network interface is used to receive data from the ATCA crate and supports a low latency, reliable TTL trigger acknowledge interface to the trigger DPM. This PC hosts the SVT control and monitoring software as well as the Read Out Controller application used to interface with the JLab DAQ.

In order to minimize cable length for the analog APV25 output signal the ATCA crate was located approximately 1 m from the beam line, next to our cable vacuum feed-throughs. Before shielding with lead-blankets and borated polyethylene was arranged, we observed two failures of normally reliable ATCA crate power supplies, time-correlated to beam instabilities.

Although trigger rates during the HPS Test Run were significantly lower, this system was tested at trigger rates up to 20 kHz and 50 MB/s. With optimized event blocking and improved ethernet bandwidth, together with utilizing the overlapping readout and trigger functionality of the APV25, the system is capable of being read out at 50 kHz trigger rate.

### 6.3. General Data Acquisition and Online Computing

Every crate participating in the readout process contains a Readout Controller (ROC) that collects digitized information, processes it, and sends it on to the event builder. For the ECal, both VXS crates run ROC applications in a single blade Intel-based CPU module running CentOS Linux OS. For the SVT DAQ, the ROC application runs on the external PC under RHEL. The event builder assembles information from the ROCs into a single event which is passed to the event recorder that writes it to a RAID5-based data storage system capable of handling up to 100 MB/s. The event builder and other critical components run on multicore Intel-based multi-CPU servers. The DAQ network system is a network router providing 10 Gb/s high-speed connection to the JLab computing facility for long-term storage. For the HPS Test Run, both the SVT and ECal ROC had a 1 Gb/s link to the network router.

## 7. Reconstruction and Performance

While dedicated electron beam was precluded for the HPS Test Run the short dedicated photon beam run allowed the study of some of the key performance parameters for HPS and the trigger rates expected during electron beam running. This section documents the performance and discusses the implications of these results for HPS.

### 7.1. SVT Performance

For the duration of the HPS Test Run all SVT modules and APV25 chips were configured to their nominal operating points [22] with all sensors reverse-biased at 180 V. The sensors were operated within a temperature range of 20 – 24°C. Approximately 97% of the 12,780 SVT channels were found to be operating normally; the fraction of dead or noisy channels varied from 2.4% to 4.7% throughout the HPS Test Run. Most of these losses were due to 2-4 misconfigured APV25 ASICs, a known noisy half-module and problems in two particular APV25 ASICs.

#### 7.1.1. Cluster and Hit Reconstruction

Track reconstruction in the SVT puts stringent requirement on the clustering and hit reconstruction. The multiple scattering in the tracking material dominates the uncertainty in the track parameter estimation and effectively determines the roughly 50 μm (200 μm) requirement on the spatial hit resolution in the non-bend (bend) plane. The high occupancy due to multiple scattered beam electrons in the target close to the beam requires a hit time resolution of 2 ns to efficiently reject

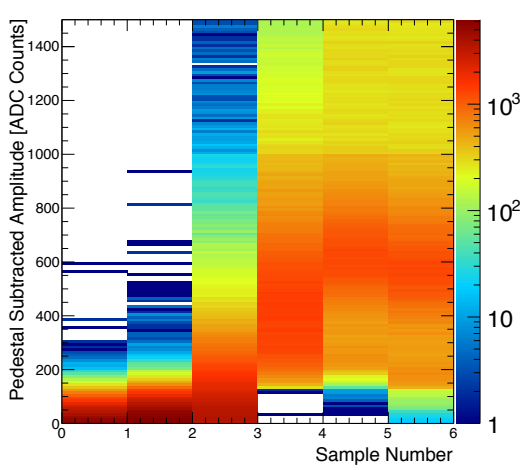


Figure 11: Accumulation of six pedestal-subtracted samples from individual SVT channels associated with hits on tracks.

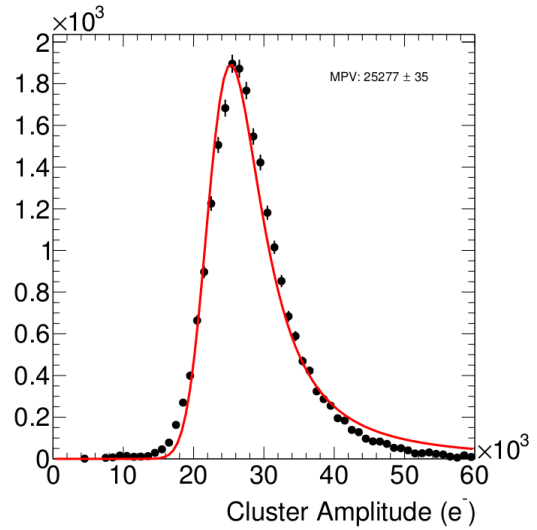


Figure 12: The cluster charge distribution for hits associated with a track follow the characteristic Landau shape.

672 out-of-time hits in HPS. Both the hit time, based on a  
 673 fit to the APV25 ASIC pulse shape, and the spatial position  
 674 reconstruction rely on having S/N around 25 for  
 675 the sensors used in HPS.

676 After a trigger is received, the amplitude of every  
 677 APV25 is sampled and digitized in the six consecutive  
 678 time bins associated with the trigger time. A data reduction  
 679 algorithm is applied requiring three out of six sam-  
 680 ples to be above two times the noise level and that the  
 681 third sample is larger than the second or that the fourth  
 682 sample is larger than the third. The typical, pedestal  
 683 subtracted, pulse shape obtained is shown in Figure 11.  
 684 As the figure demonstrates, the SVT was well timed-  
 685 in to the trigger with the rise of the pulse at the 3rd  
 686 sampling point. In order to find the time,  $t_0$ , and am-  
 687 plitude of each hit, the six samples from each channel  
 688 are fitted to an ideal  $CR - RC$  function. Note that in the  
 689 HPS Test Run the APV25 ASICs were operating with  
 690 a 50 ns shaping time. These hits are passed through  
 691 a simple clustering algorithm which forms clusters by  
 692 grouping adjacent strips with the position of a cluster on  
 693 the sensor determined by the amplitude-weighted mean.  
 694 With a linear gain up to  $\approx 3$  MIPs, the cluster charge  
 695 for hits associated with a track follow the character-  
 696 istic Landau shape, see Figure 12. A noise level be-  
 697 tween  $1.1 - 1.5 \times 10^3$  electrons was established through  
 698 multiple calibration runs giving a signal to noise ratio  
 699 of  $21 - 25$ , in line with the requirement for HPS. Ra-  
 700 dioactive source tests were used to provide the abso-  
 701 lute charge normalization. After clustering hits on a

702 sensor, the hit time for each cluster is computed as the  
 703 amplitude-weighted average of the individually fitted  $t_0$   
 704 on each channel. The  $t_0$  resolution is studied by com-  
 705 paring the cluster hit time with the average of all cluster  
 706 hit times on the track shown in Figure 13. After cor-  
 707 recting for offsets from each sensor (time-of-flight and  
 708 clock phase) and accounting for the correlation between  
 709 the  $t_0$  and track time, the extracted  $t_0$  resolution is 2.6 ns.  
 710 This is somewhat worse than the approximately 2 ns res-  
 711 olution expected for S/N=25 which we attribute to the  
 712 true pulse shape differing from our idealized fit function  
 713 which will be improved in the future [23]. Reducing the  
 714 APV25 ASIC pulse shaping time to 35 ns will also im-  
 715 prove time resolution. These results show that we can  
 716 operate with the six sample readout mode of the APV25  
 717 chip and achieve time resolution adequate for pileup re-  
 718 jection during electron running in HPS.

719 Good agreement was obtained between observed and  
 720 simulated occupancies after taking into account dead or  
 721 noisy channels. The hit reconstruction efficiency was  
 722 estimated by measuring the number of good tracks with  
 723 a hit close to the interpolated position on a given sen-  
 724 sor that was excluded from the track fit. Tracks which  
 725 intersect regions with known bad channels or pass very  
 726 close to the edge region were excluded. The hit recon-  
 727 struction efficiency, see Figure 14, was measured to be  
 728 above 98% and fairly uniform across the SVT.

729 The spatial resolution of similar microstrip sensors is  
 730 well established by test beam data, against which the

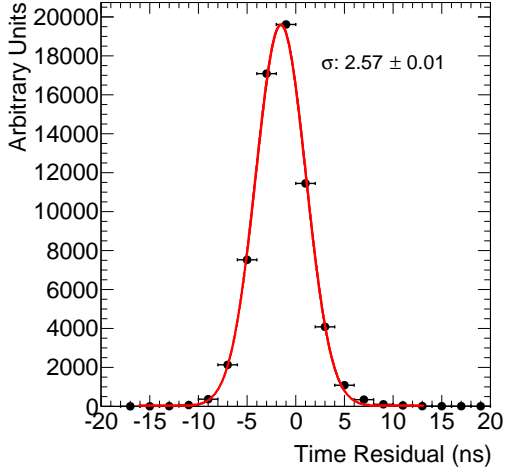


Figure 13: The residual of individual cluster times with the average of all clusters on the track.

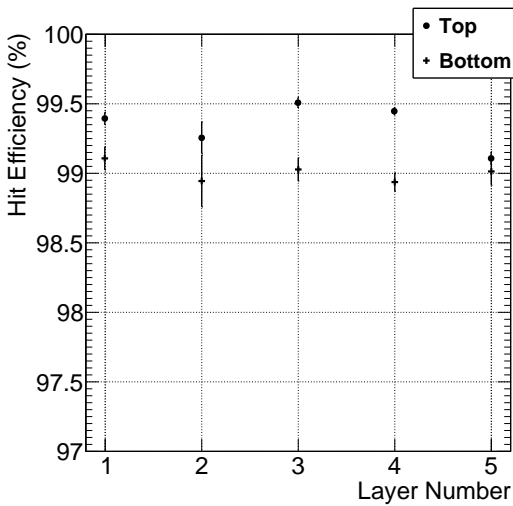


Figure 14: The hit reconstruction efficiency as a function of detector layer.

charge deposition model in the simulation is validated. This resolution can be parameterized as a function of the total signal to single-strip noise and the crossing angle of tracks through the sensor. The single-hit resolution for charged particles with signal-to-noise ratio above 20, as demonstrated here, is relatively constant at approximately  $6 \mu\text{m}$  for tracks that enter approximately normal to the sensors as in HPS. This resolution is significantly better than the requirement for reaching the mass and vertex resolutions required for HPS.

#### 7.1.2. Momentum and Vertexing Resolution

Good track reconstruction performance is crucial to HPS. Simulations show that track momentum resolution of 4-5% is needed to achieve the desired  $A'$  mass resolution. The precise reconstruction of the production vertex to reject prompt QED background requires impact parameter resolutions between  $100\text{-}250 \mu\text{m}$  for tracks between  $0.5\text{-}1.7 \text{ GeV}/c$ . These key performance parameters were studied in the HPS Test Run by selecting  $e^+e^-$  pairs from photon conversions. Pairs of oppositely charged tracks, one in the top and one in the bottom half of the SVT, with momentum larger than  $400 \text{ MeV}/c$  were selected and basic distributions of pair production kinematics were studied. The kinematics are relatively well reproduced as shown in Figure 15.

The expected momentum resolution from simulation is between 4-5% for tracks in the momentum range of the HPS Test Run. By comparing the shapes of the kinematic distributions for data and simulation, we estimate an agreement with the nominal scale and resolution to within 10%.

In the HPS Test Run, as well as in electron running with HPS, the dominant source of uncertainty in the tracking and vertexing is multiple Coulomb scattering. For the vertexing performance the foremost difference between the HPS Test Run and HPS is that the HPS Test Run target is 67 cm further upstream, so tracks must be extrapolated nearly eight times as far as in HPS, giving almost collinear tracks in the detector. The increased lever arm over which tracks are extrapolated worsens the resolution up to a factor of eight (depending on momentum) compared to what is achieved at the nominal electron target position for HPS. Figure 16 shows the horizontal and vertical positions of the extrapolated track at the converter position. While residual alignments show small shifts, the good agreement between data and simulated events of the widths indicates a good understanding of the material budget and distribution in

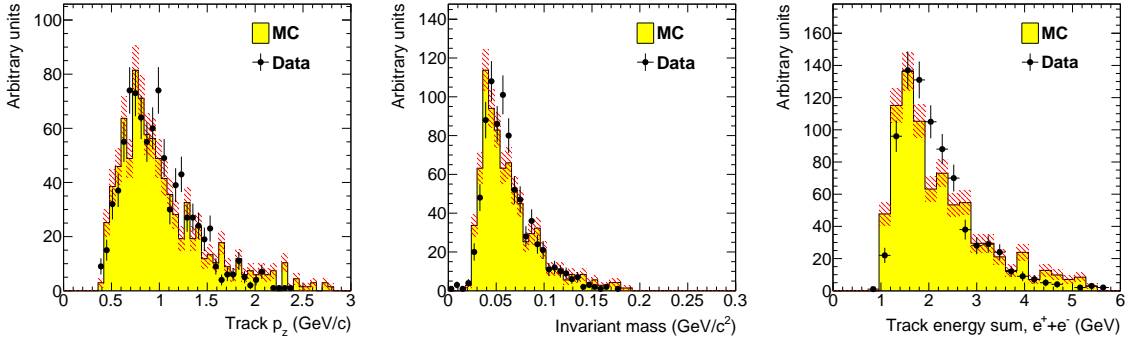


Figure 15: Kinematic distributions for  $e^+e^-$  pairs selected by opposite charged tracks in the top and bottom half of the tracker: track momentum in the top half of the SVT (left), invariant mass (middle) and the sum of the track energy for the pair (right).

the SVT. Having the dominant contribution to the vertex resolution approximately right demonstrates that the Gaussian part of the vertex resolution in HPS, with a target at 10 cm, will be as calculated.

### 7.2. ECal Performance

During the HPS Test Run 385 out of 442 modules (87%) were used in offline reconstruction, 39 modules were disabled or not read out (no FADC channel available, no APD bias voltage or masked out due to excessive noise) and 18 were masked offline due to noise.

The integrated pulse of each FADC channel was converted to energy by subtracting a pedestal and applying a conversion factor to convert ADC counts to energy. The pedestals are measured using special runs where each trigger records 100 samples of signals from the APDs with 4 ns between each sample. The pedestals were extracted from the part of the window before the actual hit in the calorimeter. Modules with signal above the threshold are clustered using a simple algorithm similar to the one deployed for the trigger (see Sec. 6.1). Due to the high effective crystal readout threshold of 73 MeV the average number of crystals in a cluster was only about three and the simple clustering algorithm worked well for reconstruction of the detected shower energy. An average noise level of approximately 15 MeV per crystal was measured in special pedestal runs. The high crystal noise level and effective threshold didn't hurt the trigger rate studies in the HPS Test Run as clusters with high energy were used for the analysis. For HPS the noise level and threshold will be lowered to improve energy resolution and to allow triggering on cosmics to improve calibration.

The ratio of the ECal cluster energy  $E$  to the momentum  $p$  of a matched track in the SVT was used to determine the conversion factors from ADC counts to en-

ergy. To compare data and simulation, all inoperable or noisy channels in the SVT and ECal were disabled in both data and simulation so that any efficiency or bias that affect the data should be reflected in the simulation. Iteratively, conversion coefficients for each crystal were adjusted until the  $E/p$  ratio in data and simulation were similar. The distribution of the  $E/p$  ratio in data and simulation are compared in Figure 17. The peak of the distribution, at  $E/p \sim 0.7$ , gives the sampling fraction of the ECal, the fraction of the incident particle energy measured in the cluster. The width of the distribution indicates the energy resolution, which is worse than the required  $4.5\%/\sqrt{E}$  for HPS due to high thresholds. The width in data is greater than that in simulation due to non-uniformity of the calibration of different parts of the ECal.

The A' trigger in HPS is relatively insensitive to the energy of the clusters and this level of performance would be adequate. However, improvements are needed to achieve the expected energy resolution in HPS ( $< 4.5\%/\sqrt{E}$ ). The noise and thresholds need to be closer to 10 MeV and a more elaborate calibration technique needs to be employed to suppress the large tails in the  $E/p$  distribution further. In addition, the fraction of working channels needs significant improvement.

### 7.3. Trigger Performance

As described above in Sec. 6, the energy from each crystal is determined slightly differently in the trigger and in the readout. The trigger performance was studied by simulating the trigger for each event and comparing to how the events were actually triggered. To eliminate trigger bias, we use a tag and probe method: to study the trigger performance in one half of the ECal, we select events which triggered the other half and where there was exactly one probe cluster in the ECal half under

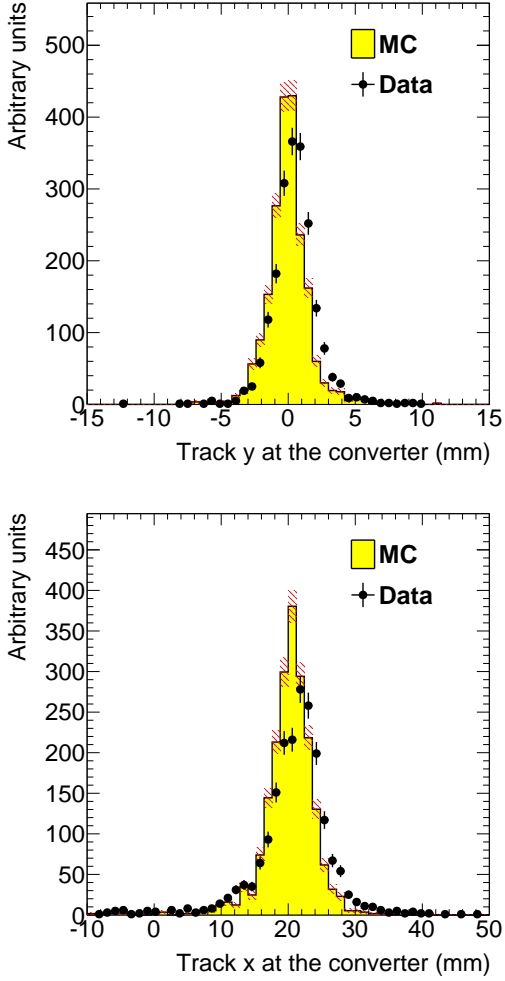


Figure 16: Vertical (top) and horizontal (bottom) extrapolated track position at the converter position taking into account the measured fringe field.

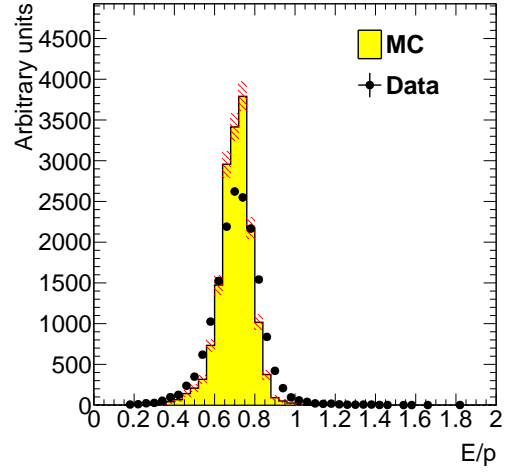


Figure 17: The ECal energy over track momentum ratio ( $E/p$ ) comparing data and simulation for single cluster triggers in the top half of the ECal.

study. We then measure trigger efficiency as the fraction of tagged events that fired the trigger in the probe half as a function of the probe cluster energy, shown in Figure 18. The trigger turn-on is slow and reaches an uneven plateau at about 700 MeV for two reasons; gain variations between different crystals lead to the threshold variations and the nonlinearity of the time-over-threshold integral means that the effective threshold is higher for clusters that span multiple crystals. The effective trigger threshold is therefore dependent on position and energy of the particle as well as cluster multiplicity. For HPS the trigger cluster threshold will be set at a lower value.

As a cross-check we simulate the FADC trigger path by converting from readout hits (with fixed-size window integration) to trigger hits (time-over-threshold integration). The CTP clustering algorithm and the trigger decision from the SSP are simulated before we compare the trigger decision and trigger time to what was reported by the actual trigger. For every event, the trigger reports the trigger decision as a bit mask (top half, bottom half or both) and the time the trigger fired. The turn-on from the trigger threshold was measured to be 1280 in units of ADC counts as expected. The threshold was not perfectly sharp because of uncertainties in the conversion from readout to trigger hits described above, but based on comparisons with simulation we found that the trigger worked exactly as specified.

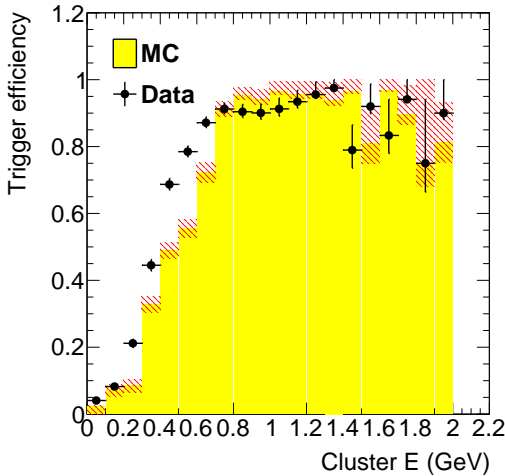


Figure 18: Trigger efficiency in both halves of the ECal for data and simulation as a function of cluster energy.

| Converter (% $X_0$ ) | <b>1.60</b>    | <b>0.45</b>  | <b>0.18</b>  |
|----------------------|----------------|--------------|--------------|
| EGS5                 | $1162 \pm 112$ | $255 \pm 28$ | $94 \pm 17$  |
| Geant4               | $2633 \pm 250$ | $371 \pm 38$ | $114 \pm 18$ |
| Observed             | $1064 \pm 2$   | $196 \pm 1$  | $92 \pm 1$   |

Table 4: Observed and predicted event rate (in Hz) normalized to 90 nA for three different converter thicknesses. The uncertainty on the prediction includes systematic uncertainties from ECal alignment, background normalization, beam current normalization and limited statistics in the simulation.

#### 7.4. Trigger Rate Comparisons

Trigger rates observed in the HPS Test Run are dominated by  $e^+e^-$  pairs produced in the converter. In simulated events, the rate of triggers depend on the modeling of the pairs' angular distribution and the subsequent multiple Coulomb scattering in the converter. Rates from different converter thicknesses are used to study the varying multiple Coulomb scattering contribution (pair production angular distribution is constant), and are compared with Geant4 [24] standard multiple scattering model and EGS5 [25]. Restricting to a well calibrated region of the ECal and to clusters with energy above the trigger turn-on, we see agreement with the rates predicted by the EGS5 simulation program after subtracting the “no converter” background , see Table 4. This gives further confidence that the dominant source of background occupancy for HPS, multiple Coulomb scattered beam electrons, is well described.

## 8. Summary and Outlook

The HPS Test Run experiment, using a simplified version of the apparatus planned for the full HPS experiment in a parasitic photon beam, demonstrated the feasibility of the detector technologies proposed for the silicon vertex tracker, electromagnetic calorimeter, and data acquisition systems. Performance from each of these subsystems has been shown to be adequate to conduct the full experiment successfully with some identified improvements. Studies of multiple Coulomb scattering tails of electrons and positrons from photon conversions further backs expectations from simulation, giving credence to estimates of the detector backgrounds expected in electron beam running for HPS.

## 9. Acknowledgements

The authors are grateful for the support from Hall B at JLab and especially the Hall B engineering group for support during installation and decommissioning. They also would like to commend the CEBAF personnel for good beam performance, especially the last few hours of operating CEBAF6. The tremendous support from home institutions and supporting staff also needs praise from the authors.

This work has been supported by the US Department of Energy, the National Science Foundation, French Centre National de la Recherche Scientifique and Italian Istituto Nazionale di Fisica Nucleare. Rouven Essig is supported in part by the Department of Energy Early Career research program DESC0008061 and by a Sloan Foundation Research Fellowship. Authored by Jefferson Science Associates, LLC under U.S. DOE Contract No. DE-AC05-06OR23177.

## References

- [1] B. Holdom, Two U(1)'s and Epsilon Charge Shifts, Phys.Lett. B166 (1986) 196.
- [2] P. Galison, A. Manohar, TWO Z's OR NOT TWO Z's?, Phys.Lett. B136 (1984) 279.
- [3] R. Essig, J. A. Jaros, W. Wester, P. H. Adrian, S. Andreas, et al. (Report of the Community Summer Study 2013 (Snowmass) Intensity Frontier New, Light, Weakly-Coupled Particles subgroup), Dark Sectors and New, Light, Weakly-Coupled Particles, 2013. URL: <http://arxiv.org/abs/arXiv:1311.0029>.
- [4] M. Pospelov, Secluded U(1) below the weak scale, Phys.Rev. D80 (2009) 095002.
- [5] O. Adriani, et al. (PAMELA Collaboration), An anomalous positron abundance in cosmic rays with energies 1.5-100 GeV, Nature 458 (2009) 607–609.

- 944 [6] M. Ackermann, et al. (Fermi LAT Collaboration), Measurement  
 945 of separate cosmic-ray electron and positron spectra with  
 946 the Fermi Large Area Telescope, Phys.Rev.Lett. 108 (2012)  
 947 011103.
- 948 [7] M. Aguilar, et al. (AMS Collaboration), First Result from the  
 949 Alpha Magnetic Spectrometer on the International Space Station:  
 950 Precision Measurement of the Positron Fraction in Primary  
 951 Cosmic Rays of 0.5350 GeV, Phys.Rev.Lett. 110 (2013)  
 952 141102.
- 953 [8] N. Arkani-Hamed, D. P. Finkbeiner, T. R. Slatyer, N. Weiner, A  
 954 Theory of Dark Matter, Phys.Rev. D79 (2009) 015014.
- 955 [9] M. Pospelov, A. Ritz, Astrophysical Signatures of Secluded  
 956 Dark Matter, Phys.Lett. B671 (2009) 391–397.
- 957 [10] J. D. Bjorken, R. Essig, P. Schuster, N. Toro, New Fixed-Target  
 958 Experiments to Search for Dark Gauge Forces, Phys.Rev. D80  
 959 (2009) 075018.
- 960 [11] A. Grillo, et al. (HPS Collaboration), Heavy Photon Search  
 961 Proposal, 2010. URL: [https://confluence.slac.stanford.edu/download/attachments/86676777/HPSProposal-FINAL\\_Rev2.pdf](https://confluence.slac.stanford.edu/download/attachments/86676777/HPSProposal-FINAL_Rev2.pdf).
- 964 [12] A. Sandorfi, et al., 2012. URL: [http://www.jlab.org/exp\\_prog/proposals/06/PR06-101.pdf](http://www.jlab.org/exp_prog/proposals/06/PR06-101.pdf).
- 966 [13] F.-X. Girod, M. Garon (CLAS), Inner calorimeter in clas/dvcs  
 967 experiment, CLAS-Note 2005-001 (2005).
- 968 [14] R. Niyazov, S. Stepanyan (CLAS), Clas/dvcs inner calorimeter  
 969 calibration, CLAS-Note 2005-021 (2005).
- 970 [15] F.-X. Girod (Universite de Strasbourg), 2006. URL: <http://www.jlab.org/Hall-B/general/thesis/fxgirrod.pdf>.
- 972 [16] I. Rashevskaya, S. Bettarini, G. Rizzo, L. Bosisio, S. Dittongo,  
 973 et al., Radiation damage of silicon structures with electrons of  
 974 900-MeV, Nucl. Instrum. Meth. A485 (2002) 126–132.
- 975 [17] D. S. Denisov, S. Soldner-Rembold, D0 Run IIB Silicon Detec-  
 976 tor Upgrade: Technical Design Report (2001).
- 977 [18] M. French, L. Jones, Q. Morrissey, A. Neviani, R. Turchetta,  
 978 et al., Design and results from the APV25, a deep sub-micron  
 979 CMOS front-end chip for the CMS tracker, Nucl.Instrum.Meth.  
 980 A466 (2001) 359–365.
- 981 [19] M. Friedl, C. Irmler, M. Pernicka, Readout of silicon strip detec-  
 982 tors with position and timing information, Nucl.Instrum.Meth.  
 983 A598 (2009) 82–83.
- 984 [20] H. Dong, et al., Integrated tests of a high speed VXS switch  
 985 card and 250 MSPS flash ADCs, 2007. doi:10.1109/NSSMIC.  
 986 2007.4436457.
- 987 [21] R. Larsen, Emerging New Electronics Standards for Physics,  
 988 Conf.Proc. C110904 (2011) 1981–1985.
- 989 [22] L. Jones, APV25-S1: User guide version 2.2, RAL Microelec-  
 990 tronics Design Group, 2011.
- 991 [23] M. Friedl, C. Irmler, M. Pernicka, Obtaining exact time infor-  
 992 mation of hits in silicon strip sensors read out by the APV25  
 993 front-end chip, Nucl. Instrum. Meth. A572 (2007) 385 – 387.
- 994 [24] S. A. et al., GEANT4 - a simulation toolkit, Nucl.Instrum.Meth.  
 995 A506 (2003) 250 – 303.
- 996 [25] H. Hirayama, Y. Namito, A. Bielajew, S. Wilderman, W. Nelson,  
 997 The EGS5 Code System, 2005.